

## NMR Observations of Entangled Polymer Dynamics: Focus on Tagged Chain Rotational Dynamics and Confirmation from a Simulation Model

Filipe Furtado, Joshua Damron, Marie-Luise Trutschel, Cornelius Franz, and Klaus Schröter

Institut für Physik, Martin-Luther-Universität Halle-Wittenberg, D-06099 Halle (Saale), Germany

Robin C. Ball

Department of Physics, University of Warwick, Coventry CV4 7AL, U.K.

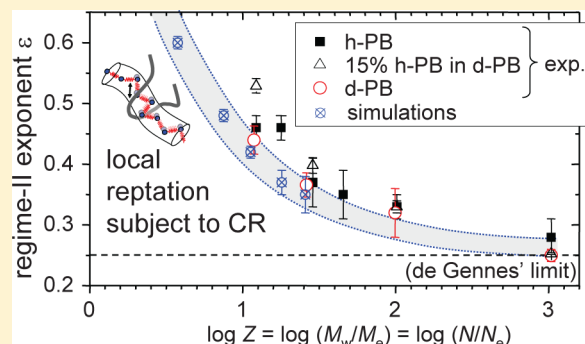
Kay Saalwächter\*

Institut für Physik, Martin-Luther-Universität Halle-Wittenberg, D-06099 Halle (Saale), Germany

Debabrata Panja\*

Institute for Theoretical Physics, Universiteit Utrecht, Leuvenlaan 4, 3584 CE Utrecht, The Netherlands, and Institute of Physics, Universiteit van Amsterdam, Science Park 904, Postbus 94485, 1090 GL Amsterdam, The Netherlands

**ABSTRACT:** Molecular-level insights into the entangled dynamics of high-molecular-weight chains, in particular of slower chain modes in regimes II–IV of the tube model, are still rare due to the lack of methods resolving the rather long associated time scales. On the theoretical side, new computer simulation methods are just reaching the relevant time scales in sufficiently large systems. Here, we confront results from a recent multiple-quantum proton NMR method with results from a novel lattice model. We address the concern that proton NMR, relying on the dipole–dipole couplings between nearby nuclei, is intrinsically sensitive not only to intrachain rotational motions which reflect the desired details of the tube model or possibly necessary modifications, but also to the translational diffusion of chains past each other via interchain dipole–dipole couplings. In order to critically assess the influence of the latter, we here present results of isotope-dilution experiments, in which the data reflect mainly tagged-chain dynamics. We find overall weak effects of interchain dipole–dipole couplings on the shape of the extracted orientation autocorrelation function and very good agreement of the experimental and the computer simulation data. We conclude that the NMR method as well as the novel lattice model faithfully reflects the universal features of entangled chain dynamics and in particular the deviations from simple tube-model predictions on a microscopic level.



### I. INTRODUCTION

The mobility of individual polymers in dense long-chain systems is slowed down progressively with chain length and density. A notable manifestation of very slow dynamics in dense polymeric systems is that their viscosity scales with their molecular weight as a power law, with the viscosity exponent  $m_\eta$  experimentally measured to be  $3.4 \pm 0.2$  over an impressive range of molecular weights and chemical compositions.<sup>1,2</sup> The fact that the slow dynamics of dense polymeric systems can actually be attributed to the polymers becoming entangled when the polymers are long has deep roots in the interpretation of polymer viscoelasticity.<sup>3</sup> The idea of an effective confining

tube was introduced by Edwards<sup>4</sup> in the context of rubber (or gel) elasticity, and the reptation dynamics of an un-cross-linked chain in such a system, confined to its tube by entanglement, was presented by de Gennes.<sup>5,6</sup> Doi and Edwards then developed the full-blown application of reptation dynamics to un-cross-linked polymer melts to give a coherent model of diffusion and rheology of entangled polymers.<sup>7–9</sup> The dynamics of a melt can be quantitatively understood by taking the

**Received:** October 24, 2013

**Revised:** December 10, 2013

**Published:** December 19, 2013

entanglement idea to analyze the motion of a single polymer in a melt, as in the tube theory<sup>5,10</sup>—referred to as the tagged polymer henceforth. In the absence of external forces, the tagged polymer is set in motion by thermal fluctuations. Of these, the transversal ones, i.e., the fluctuations perpendicular to the contour of the tagged polymer, do not contribute to its bulk transport, since the bulk transport of the polymer in the transversal directions is blocked by the presence of the surrounding ones. Longitudinal fluctuations, on the other hand, cause transport of stored lengths within its contour as well as enable its ends to extend or retract its contour. The ends of the tagged polymer, thus, explore new areas via longitudinal fluctuations, eventually resulting in bulk transport over long distances.

In order to critically test tube theory as well as its variants that include additional relaxation mechanisms of the tube itself to account for actual rheological data, such as constraint release (CR) and contour length fluctuations (CLF),<sup>11–15</sup> it is mandatory to confront the predictions with microscopic experimental observations or suitable computer simulations. The most prominent experimental techniques providing access to observables related to the motion of individual segments subject to the tube constraint and reptation are dielectric spectroscopy,<sup>16,17</sup> neutron scattering techniques,<sup>18,19</sup> and NMR spectroscopy.<sup>20–30</sup> In all these techniques, the observation of local details of rotational or translational dynamics of segments in tagged chains is possible, sometimes using suitable labeling strategies.

Techniques that are sensitive to the mean-square displacement of chain segments, such as neutron spin echo,<sup>18,19</sup> pulsed-gradient NMR spectroscopy,<sup>20</sup> and most recently also field-cycling  $T_1$  NMR relaxometry,<sup>28,30</sup> enjoy good support in terms of well-developed theoretical treatments of their respective observables. In contrast, the theoretical description of segmental orientation correlations in entangled chains lags behind, possibly also because a critical mass of reliable data was not available until recently.<sup>22,24–27,29</sup> We use a specific multiple-quantum (MQ) NMR technique<sup>21,31</sup> that relies on the orientation dependence of certain spin interactions such as the dipole–dipole or the quadrupolar coupling among the protons ( $^1\text{H}$ ) or between deuterons ( $^2\text{H}$ ) and the local electric field gradient, respectively. Complementary data can be obtained from  $^1\text{H}$  field-cycling NMR  $T_1$  relaxometry.<sup>22,24,27,29</sup> Analytical predictions for the main observable of both techniques, i.e., the normalized time ( $\tau$ )- and ensemble (ens)-averaged tensorial segmental orientation autocorrelation function (OACF)

$$C(t) = S \langle P_2(\cos \theta(t + \tau)) P_2(\cos \theta(\tau)) \rangle_{\tau, \text{ens}} \quad (1)$$

$\theta$  being the segmental orientation relative to a reference direction (i.e., the external magnetic field), have so far only been published by de Gennes for what is now referred to as regime II motion<sup>5</sup> and by Ball, Callaghan, and Samulski comprehensively for the unmodified tube model across regimes I–IV.<sup>32</sup> Here  $P_2(x) = (3x^2 - 1)/2$  is the second Legendre polynomial. The prediction of  $C(t)$  for the tube model, in comparison with a more standard quantity, i.e., the mean-square displacement  $\langle [r(t) - r(0)]^2 \rangle$  of a tagged monomer, is shown in Figure 1, where the entanglement, Rouse, and tube renewal times scale with the molecular weight  $M$  as  $\tau_e \sim M^0$ ,  $\tau_R \sim M^2$ , and  $\tau_d \sim M^3$ , respectively.

Our recent work,<sup>25,26</sup> in agreement with the field-cycling NMR approach of Rössler<sup>22,24,27,29</sup> as applied to fully

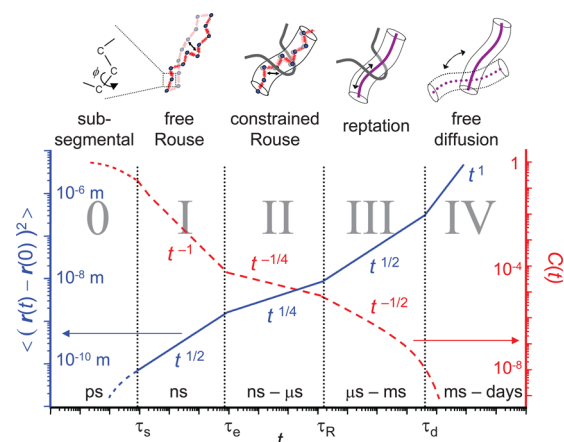


**Figure 1.** Dynamical regimes and the crossover times as predicted by the tube model, shown for the mean-square displacement  $\langle [r(t) - r(0)]^2 \rangle$  of a tagged monomer (solid line), and the normalized segmental OACF  $C(t)$  (dashed line). The transitions between the regimes occur at the segmental ( $\tau_s$ ), entanglement ( $\tau_e$ ), Rouse ( $\tau_R$ ), and disentanglement ( $\tau_d$ ) times. Adapted from ref 26.

protonated samples, has shown some level of agreement with the predictions concerning the identification and molar mass dependence of the regime II–III and III–IV transition times. However, all together they reveal clear-cut disagreement for the time scaling exponents in regimes I and II, predicted to be  $-1$  and  $-1/4$  for the tube model. In particular, Rössler and co-workers<sup>22,24,27,29</sup> found a predominance of around  $-0.85$  (instead of  $-1$ ) in regime I, and both groups<sup>25–27</sup> found a molecular weight-dependent effective exponent  $-\varepsilon$  in regime II that asymptotically approaches  $-1/4$  only for  $M/M_e \gtrsim 1000$ .

Using isotope dilution experiments to selectively probe tagged chain segments in invisible matrix chains of different molecular weight, our first results indicated a surprising influence of CR effects on the observations concerning regime II motions<sup>25</sup> (rather than just changes of the terminal time). Recently, these observations have been qualitatively validated by large-scale computer simulations, comparing molecular dynamics with coarse-grained slip-springs simulations,<sup>33</sup> stressing the particular sensitivity of the NMR-detected  $C(t)$  to CR effects.

However, isotope dilution experiments in field-cycling NMR have revealed a rather large influence of interchain dipole–dipole couplings and translational dynamics,<sup>23,28,30,34,35</sup> raising the question whether  $^1\text{H}$  NMR can be used at all to extract meaningful information on tagged-chain dynamics. Recent theoretical arguments<sup>36,37</sup> and our earlier results<sup>25</sup> suggest the effect on our specific method, which is based upon coherent rotating-frame spin evolution<sup>38</sup> rather than incoherent laboratory-frame  $T_1$  relaxation, to be comparably weak. Yet, a detailed assessment is missing.

Here, we thus extend our earlier studies, focusing on the significance of deviations from the fixed-tube model observed on a molecular level, addressing (i) the robustness of the experimental finding with regards to a clean detection of segmental rotations in tagged chains by NMR and (ii) a direct comparison of experimental data with new large-scale computer simulation results. The first question will be addressed by help of  $^1\text{H}$ -based experiments on mixtures of protonated and perdeuterated polymers and analogous  $^2\text{H}$ -based experiments that yield strictly intramolecular results representative of tagged chains.

On the simulation side, the mentioned previous work<sup>33</sup> did not comprise a systematic variation of molecular weights and a quantitative mapping on the NMR results, which is presented herein. The simulations have been performed with the (FCC) lattice polymer model described in ref 39; it combines a very high computational efficiency with realistic polymer dynamics, allowing one to reach long length and time scales. Some of us have used this model to simulate the dynamics of self-avoiding Rouse polymers,<sup>40</sup> polymer translocation under a variety of circumstances,<sup>41–44</sup> and the dynamics of polymer adsorption,<sup>45</sup> while others have used it to simulate the diffusion and exchange of polymers in an equilibrated layer of adsorbed polymers,<sup>46</sup> denaturation dynamics of double-stranded polymers,<sup>47,48</sup> and compaction of circular polymers.<sup>49</sup> We stress here that from these studies we are not aware of any lattice artifacts of the simulation model.

The structure of this paper is as follows. In section II we detail the experimental procedures and discuss the model used to simulate polymer melts. In section III we compare and discuss the results and conclude it in section IV. We finally discuss the experimental issues of the time–temperature superposition procedure that is inherent to the NMR approach and a comparison between the different NMR methods in the Appendix.

## II. MATERIALS AND METHODS

**A. Experimental Procedures. Samples.** Narrowly dispersed 1,4-(*cis/trans*)-PB samples, with polydispersities ranging between 1.01 and 1.07, were purchased from Polymer Standards Service GmbH (PSS, Mainz, Germany); see ref 26 and Table 1 for more details. The sample names include the approximate  $M_w$  in Da (measured by GPC as supplied by the provider) and whether they are hydrogenated (h-PB) or fully deuterated (d-PB). The distribution of *cis:trans:vinyl* units was typically around 50%:42%:8%, respectively, commonly found for anionically synthesized samples. The vinyl content (5–10%) is most important, as it influences the  $T_g$  of the materials and thus the parameters for time–temperature superposition<sup>51</sup> (see below). The samples were placed in evacuated and flame-sealed NMR tubes and were kept in the refrigerator at 4 °C before and after the measurements. Isotope mixtures were prepared by solution blending using toluene as solvent and subsequent thorough solvent removal *in vacuo* at around 50 °C.

**Table 1. Relevant Parameters of the Studied Samples and the Simulated Polymers<sup>a</sup>**

sample	$\bar{M}_w$ (kDa)	$N$	$Z$
h-PB 24k	23.6	221	12.3
d-PB 23k	22.8	213	11.8
h-PB 55k	55.3	517	28.7
d-PB 50k	50.3	470	26.1
h-PB 196k	196	1832	101.8
d-PB 191k	191	1785	99.2
h-PB 2200k	2190	20467	1137
d-PB 2000k	2000	18691	1038
box size			
simulation (sim)	60 <sup>3</sup>	750	3.75
sim	60 <sup>3</sup>	1500	7.5
sim	60 <sup>3</sup>	2250	11.3
sim	120 <sup>3</sup>	3600	18
sim	160 <sup>3</sup>	5120	25.6

<sup>a</sup> $N$  denotes the number of statistical segments or the length in lattice units, respectively, and  $Z = N/N_e$  is the number of entangled units with  $N_{e,PB} \approx 18^{50}$  and  $N_{e,sim} \approx 200$ .

**MQ NMR.** NMR experiments were performed on Bruker Avance III spectrometers at <sup>1</sup>H Larmor frequencies of 200 MHz ( $B_0 = 4.7$  T) and 400 MHz (9.4 T), and a <sup>2</sup>H Larmor frequency of 61.4 MHz (9.4 T), using static probes with a temperature control based upon a heated or cooled air or nitrogen flow covering a temperature range between 230 and 400 K with an accuracy of about 0.5 K. We note that previous studies have been performed on low-field spectrometers,<sup>25,26</sup> yet the low signal in isotopically diluted samples and the use of the <sup>2</sup>H nucleus required working at high field. The MQ experiment used for <sup>1</sup>H is based on the pulse sequence published by Baum and Pines<sup>52</sup> and is described in detail elsewhere.<sup>31</sup> Basically, it excites all even quantum orders among the many protons by relying on residual dipole–dipole couplings, thus probing their intrinsic orientation dependence. Using appropriate phase cycling, the pulse sequence yields an intensity buildup curve dominated by double-quantum (DQ) coherences ( $I_{DQ}$ ) and reference decay curve ( $I_{ref}$ ) as a function of pulse sequence time  $\tau_{DQ}$  which is incremented in small steps by adjusting either the interpulse spacings or the number of pulse sequence cycles. Both incrementation schemes were combined to assemble a sufficiently well-resolved time axis.

Because of formally identical Hamiltonians, the same experiment can also be applied to excite DQ coherences in single <sup>2</sup>H nuclei,<sup>31,53–55</sup> then relying on the residual quadrupole coupling. However, in this case, the very favorable properties of the Baum–Pines MQ sequence with its clean DQ Hamiltonian are not relevant, enabling the use of the simpler three-pulse segment for DQ excitation and reconversion.<sup>56</sup> It consists of the DQ evolution delay flanked by two 90° pulses, with a refocusing 180° pulse in the center for chemical-shift and offset compensation. The advantage of this experiment is the better time resolution due to the much shorter basic cycle time.

The NMR experiments allow us to measure, directly in the time domain, the orientation autocorrelation function (OACF) of the segmental orientation

$$C(t) = 5\langle P_2(\cos \theta(t + \tau))P_2(\cos \theta(\tau)) \rangle_{\tau, \text{ens}} \propto I_{nDQ}(t = \tau_{DQ})/\tau_{DQ}^2 \quad (2)$$

where  $\theta$  is the segmental orientation relative to the external magnetic field. Equation 2 also demonstrates that  $C(t)$  is directly measured by the MQ experiment, where  $I_{nDQ}(\tau_{DQ})$  is a normalized signal function that is directly derived from the above-mentioned experimental  $I_{DQ}(\tau_{DQ})$  and  $I_{ref}(\tau_{DQ})$  signal functions, being corrected for incoherent relaxation effects. The second line of eq 2 represents a short-time approximation, the validity of which was tested previously.<sup>38</sup> The time range is therefore restricted to  $\tau_{DQ}$  between some tens of microseconds (limited by the pulse sequence) and about a 1 ms.

In order to probe the complete  $C(t)$  over many decades in time, time–temperature superposition (TTS) must be applied. This is achieved by referencing  $\tau_{DQ}$  to the entanglement time

$$\tau_e(T) \simeq \frac{\xi(T)b^2N_e^2}{\kappa k_B T} = \tau_s(T)N_e^2 \quad (3)$$

where  $\xi(T) = \xi_0 \exp\{\alpha(T - T_{VF})\}^{-1}$  is the monomeric friction coefficient ( $\alpha = 7.1 \times 10^{-4} \text{ K}^{-1}$ ,  $\xi_0 = 1 \times 10^{-14} \text{ N s/m}^2$ ),  $b = 0.96 \text{ nm}$  is the Kuhn segment length,  $\kappa$  is a model-dependent numerical factor (we use  $\kappa = \pi$ ),  $N_e = 18$  is the number of segments in an entangled strand, and  $T_{VF} = 126 \text{ K}$  is the Vogel–Fulcher temperature which is around 48 K lower than  $T_g \approx 174 \text{ K}$  for the case of PB in the temperature range of interest.<sup>51</sup> For details concerning the data analysis, the underlying assumptions, and references to the numerical values, we refer to ref 26. The use of a rheological literature value for  $\xi(T)$  may introduce systematic errors into the data analysis, and further, previously reported weak isotope effects on the segmental relaxation time  $\tau_s$ <sup>28</sup> when working with isotope mixtures or deuterated samples may play a role. We address these issues in Appendix A and demonstrate that the TTS approach is rather robust, leading to only minor uncertainties in the extracted  $C(t)$ .

It is finally noted that the results from the <sup>1</sup>H and <sup>2</sup>H variants differ somewhat conceptually (quantum mechanically), as they probe



different local directions. The former probes an effective dipolar tensor representing the orientation of a Kuhn segment, which is a homogeneous preaveraged quantity representing the action of multiple pair couplings,<sup>57</sup> while the latter probes an inhomogeneous superposition of preaveraged quadrupolar tensors that may differ due to different orientations of the different C–<sup>2</sup>H bonds (corresponding to the principal axis of the local electric field gradient tensor) in the monomer. This has an impact on the normalization of the data to  $C(t \rightarrow 0) = 1$ , which should in principle characterize the immobile glassy state. While a consistent calibration is possible for the case of <sup>1</sup>H,<sup>25,57</sup> a similarly quantitative assessment for <sup>2</sup>H is still missing. Methodological and conceptual details of the <sup>2</sup>H experiment are thus deferred to a future publication; in the present context, we just note that both approaches yield equivalent results apart from an unknown prefactor in  $C(t)$  as probed by <sup>2</sup>H.

**B. Computer Simulation Model.** In the simulation model the polymers consist of a string of monomers. Monomers are located in lattice sites. Polymer chain contours are self- and mutually avoiding; multiple occupation of lattice sites is not allowed, except for a string of monomers in sequence belonging to the same chain (e.g., monomers 5, 6, 7, 8, 9, 10 of one chain can occupy the same site, but 5, 6, 7, 8, 10 cannot as the latter breaks the sequence). The chains move through a sequence of random single-monomer hops to neighboring lattice sites. These hops can be along the contour of the chain, thus explicitly providing reptation dynamics. They can also change the contour “sideways”, providing Rouse dynamics. The individual moves maintain detailed balance at all times. Note that allowing multiple occupation of the same site by a string of in-sequence monomers belonging to the same chain is a prerequisite of the explicit reptation moves. This does not alter the fundamental properties of polymers in any way,<sup>40</sup> including fluctuation–dissipation theorems and generalized Langevin equation formulation for polymer dynamics.<sup>58,59</sup> A two-dimensional version of the simulation model is illustrated in Figure 2.

The time scale is set such that statistically once per unit of MC time, which is henceforth simply defined as time in the model, each monomer attempts to move along the contour, as well as sideways,

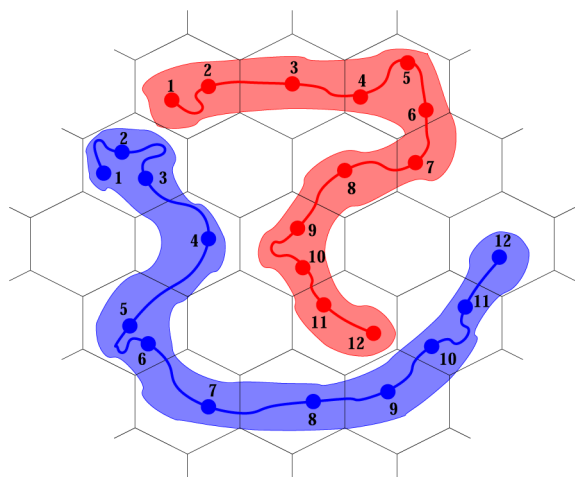


**Figure 2.** Illustration of the two-dimensional version of the lattice polymer model. Polymer chains are shown by darker colors and their contours in lighter colors. In the upper chain, interior monomers 2, 4, 6, 9, 10, and 11 can either move along the contour, or move sideways; monomer 7 can join either 6 or 8; the end monomers 1 and 12 can move to any empty nearest-neighbor site. In the lower chain, interior monomers 3, 5, 6, 10, and 11 can either move along the contour or move sideways; monomer 1 can move to any empty nearest-neighbor site, and monomer 12 can join its neighbor 11. In this configuration, because of the self- and mutually avoiding property of the chains, all other monomers cannot make a move. Statistically once per unit of time, each monomer attempts to move up and down along the contour as well as sideways.

stretching or contracting the backbone. The simulation model is similar to the bond fluctuation model (BFM),<sup>60</sup> with the important difference related to the explicit reptation moves. In the lack of these explicit reptation moves, the BFM encounters ergodicity problems and jamming at high monomeric densities, while our model is immune to these.

In detail, the simulations proceed as follows. We employ homopolymer systems with polymer lengths between  $N = 750$  and  $5120$ , with adapted lattice box sizes as indicated in Table 1. All boxes have periodic boundary conditions in all three directions. Initially, crumpled-up chains are placed on randomly chosen (but non-overlapping) lattice sites. The system is then brought to equilibrium by letting it evolve in time. The number of melt chains is chosen to match an overall monomer density unity. After equilibration, overall approximately 44% of the sites typically remain empty, due to the possibility that adjacent monomers belonging to the same chain can occupy the same site. We have not found any systematic variations in the percentage of empty sites with  $N$ ; the variations are statistical and are less than 1% in magnitude.

The CPU benchmarking of the code used, in particular, the times associated with the elementary reptation and sideways moves, can be found in ref 39, written in 2004, although we acknowledge that in the intervening years the computers have evolved substantially. Directly relevant to this paper for the  $N = 5120$  case ( $160^3$  lattice box size), evolving the entire system for a unit MC time requires 8 192 000 (one-half explicit reptation and the other half sideways) elementary moves. On a standard 64-bit linux desktop these moves were executed in 1.47 s, requiring  $\approx 183$  ns per move on average.

After equilibration, a long sequence of system snapshots are stored, separated by a regular time interval. In the first set, the “long time set”, the time difference  $\Delta t$  between consecutive snapshots of the time series is chosen to be 10 000 units of time. In the second set, the “short time set”, the time difference between consecutive snapshots of the time series is chosen to be 200. In order to improve statistics, a multiple number of such systems are studied. The long- and short-time data for the relevant variable for the tagged chain are respectively averaged over these independent simulations and then merged together. The simulation data we report in this paper are typically averaged over  $\sim 2000$  independent chains for each value of  $N$ .

### III. RESULTS AND DISCUSSION

**A. Measurement and Analysis of the Segmental OACF of Tagged Chains.** NMR results for the segmental OACF, plotted vs a normalized time, are shown in Figure 3. In order to separate intra- and interchain contributions to  $C(t)$ , we have employed a common isotope dilution strategy, where the addition of deuterated matrix chains should effectively remove the interchain contribution. The data complement our previous findings,<sup>25</sup> where we have only studied one sample diluted to 15%.

The major effect of interest is the drop in the amplitude of  $C(t)$ , as the protonated chains probed are diluted among deuterated chains. Using an empirical fit (see inset), we find an amplitude reduction by a factor of 0.53 in the limit of infinite dilution. At the entanglement time  $\tau_e$ ,  $C(t = \tau_e) = S_e^2$  reflects the square of the residual segmental order parameter as arising from entanglement constraints, specifically,  $S_e \approx 3/5N_e$ , where  $N_e$  is the number of segments in an entangled strand.<sup>25,26</sup> Given the limitations of our absolute-value calibration of  $C(t)$ ,<sup>26</sup> the derived  $N_{e,\text{exp}} \approx 13$  was found to be in reasonable agreement with the literature value of around 18. Now it can be argued that  $N_{e,\text{exp}}$  is to be up-corrected by  $0.53^{-0.5} \approx 1.4$  to account for the initially overestimated  $C(t = \tau_e)$  when interchain dipole–dipole couplings are not accounted for. Nevertheless, we consider the now perfect agreement with the literature value a coincidence, as its estimation is based upon a number of assumptions.<sup>61</sup>

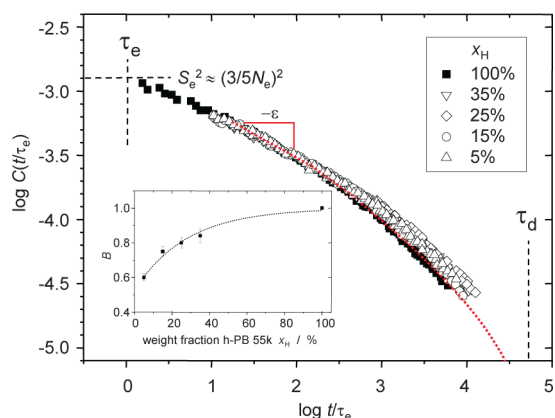


**Figure 3.** Segmental OACFs  $C(t)$  of h-PB 55k in bulk (solid squares) and diluted in a deuterated matrix polymer, d-PB 191k, to the indicated weight fractions  $x_H$  (open symbols). The latter have been rescaled along  $y$  by dividing through a factor  $B$  to match the former in the initial part. The data covers regimes II and III of the tube model with the indicated respective transition times (dashed vertical lines) as extracted from fits (dotted lines) to  $C(t)$  on a double-logarithmic scale.<sup>25,26</sup> The values of  $B$  are shown in the inset and fitted empirically to  $B = 1 - b_0 \exp\{-x_H/\xi\}$ , with parameters  $b_0 = 0.47$ ,  $\xi = 28\%$ . Note that the use of a higher matrix  $M_w$  was a consequence of limited availability of a better matching sample. The use of a longer matrix leads to only slight (yet significant) shape changes of  $C(t)$  discussed in ref 25 while not affecting the result for  $B$ .

The general shape of  $C(t)$  is only slightly (yet significantly) affected. In our previous work,<sup>25,26</sup> the main focus was the extraction of relevant parameters from the  $C(t)$ . These parameters change only slightly upon removal of the interchain contributions. An in-depth assessment of the changes in the regime transition times is deferred to a future publication, where we will specifically focus on independent variations of the  $M_w$  of hydrogenated tagged chain and deuterated invisible matrix chains. In the following, we concentrate on the regime II exponent  $\varepsilon$ , which is predicted to have value  $1/4$  by the tube model.<sup>6</sup>

Figure 4a shows a comparison of  $C(t)$  measured on h-PB 196k in bulk and diluted to 15% and on d-PB 191k probed by  $^2\text{H}$  NMR. We observe only very weak changes in the regime II exponent  $\varepsilon$ , which is determined as the value characterizing the flattest part of the curve using a derivative method discussed below in the context of the simulation data. Figure 4b shows the extracted  $\varepsilon$  in comparison with (partially reanalyzed) data from previous studies<sup>24–26,24,28</sup> and the simulations, to be addressed in the next sections, as a function of the entanglement number  $Z$ . The experimental data were previously concluded to reflect the largely protracted transition to idealized entangled dynamics,<sup>25,26,24</sup> and the deviations were attributed to CR effects.<sup>25,33</sup>

Notably, the  $\varepsilon$  values found for the isotopically dilute case, and for the case of pure intra (tagged) chain dynamics as probed by  $^2\text{H}$  NMR, are somewhat lower. In fact, the values found for  $Z = 1000$  PB ( $M = 2000\text{K}$ ) now match the tube model prediction,<sup>5</sup> perfectly in tune with findings from rheology, where the mass scaling exponent of the melt viscosity was claimed to reach the classic prediction of 3 at  $Z \approx 200$ .<sup>2</sup>

The weak overall shape changes of  $C(t)$ , and in particular the values for  $\varepsilon$  observed for pure tagged-chain dynamics by  $^2\text{H}$  NMR, stand in contrast to theoretical predictions<sup>23,34</sup> and experimental observations<sup>23,28</sup> for corresponding results

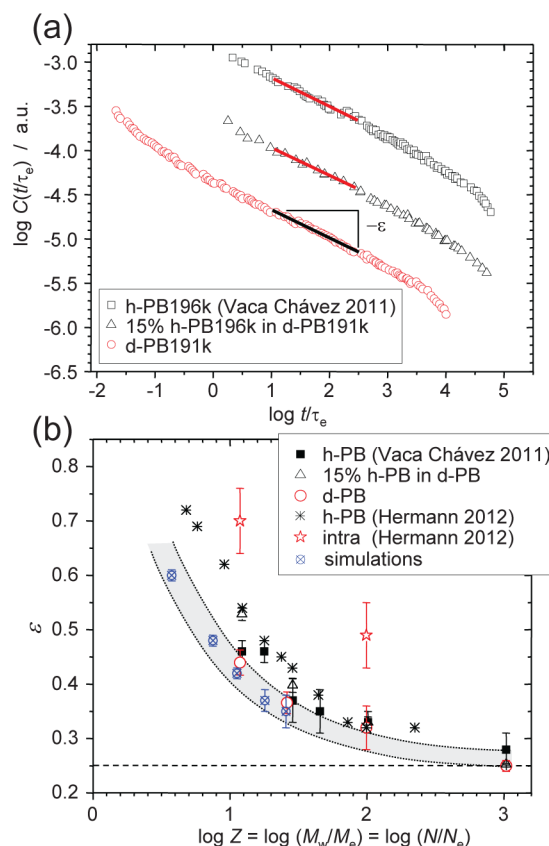


**Figure 4.** (a)  $C(t)$  of h-PB 196k in bulk, diluted to 15% in d-PB 191k, and of bulk d-PB 191k (as probed by  $^2\text{H}$  NMR) on an arbitrary  $y$  scale, offset by one decade each for clarity. (b) Regime II scaling exponents  $\varepsilon$  as a function of scaled molecular weight  $Z = M_w/M_e = N/N_e$  from our previous publications<sup>25,26</sup> (solid squares, reanalyzed), this work (open triangles and circles: experimental; crossed circles: simulated), and from  $^1\text{H}$  and  $^2\text{H}$  field-cycling  $T_1$  relaxometry<sup>24,28</sup> (asterisks and open stars, respectively). The dashed line indicates de Gennes' prediction,<sup>5</sup> and dotted lines just guide the eye, marking an uncertainty interval of  $\sim 50\%$  and  $\pm 0.02$  in  $Z$  and  $\varepsilon$ , respectively.

derived from  $^1\text{H}$   $T_1$  NMR relaxometry, which are also shown in Figure 4b. Based on the near-perfect agreement of our findings with previous simulations<sup>33</sup> and the ones discussed below, this raises the question about the origin of these significant deviations.

The rather weak effects on our data are in fact expected. Very recent theoretical work of Fatkullin<sup>36,37</sup> confirms a weaker influence of interchain effects, i.e., translational diffusion, on our method as applied to protonated systems. He could show that the initial part of the relevant signal functions, being dominated by coherent spin evolution and being the part that is actually evaluated (see eq 2), is only weakly affected and that the translational diffusion mainly affects the shape of the signal functions at longer  $\tau_{\text{DQ}}$ . Analyzing and utilizing this feature will be the subject of future work.

In marked contrast,  $T_1$  is completely dominated by the interchain contribution at the lowest accessible Larmor frequencies (corresponding to probing  $C(t)$  at the longest times), which is the basis of the new and powerful option of extracting rather slow translational diffusion coefficients.<sup>28,30</sup> This renders the good agreement of our data and the initial results of Herrmann et al. for protonated systems,<sup>27</sup> which include interchain effects, even more surprising. It may be due

to a fortuitous cancellation of systematic uncertainties, but it is not fully clear at present why the  $T_1$ -based  $\varepsilon$  values for pure intrachain motion<sup>28</sup> deviate so substantially (see Figure 4b).

Closer scrutiny reveals that the  $\varepsilon$  values given by Rössler and co-workers were determined in a slightly different way, which is discussed in Appendix B. In short,  $\varepsilon$  in their approach was extracted as a scaling exponent either from a larger interval in the frequency domain or from a  $C(t)$  that must be obtained by Fourier transformation of the spectral density. It turns out that there is no direct and trivial relation between so-obtained scaling exponents. In both cases, the  $\varepsilon$  values are somewhat overestimated due to the influence of terminal dynamics toward low frequencies and long times, respectively. This places corrected  $\varepsilon$  values at the lower end of the error intervals of the open stars shown in Figure 4b.

Thus, a systematic deviation remains, and a clarification of its origin will likely have to consider the conceptual differences between the approaches; i.e.,  $T_1$  is determined by the incoherently fluctuating part of the interaction tensor, as described by the amplitude drop of  $C(t)$  from its initially high short-time value to increasingly low values toward longer times (the latter being probed at lower Larmor frequencies). In contrast, the MQ method is based upon coherent spin evolution and thus directly and sensitively probes the low and time-dependent amplitude of  $C(t)$  at long times.

#### B. Entanglement Parameters in the Simulation Model.

Stress relaxation studies on the simulation data reveal that the entanglement length for our systems  $N_e = 200 \pm 20$ , implying that the  $N$  values studied in the simulations range between  $Z = 3.75$  and  $25.6$  entanglement units. We measured stress relaxation through the Green–Kubo equilibrium autocorrelation function,<sup>62</sup> taking the stress from the standard entropic chain stress formula applied to chain segments of 10 monomers, and then interpreted the observed plateau modulus as  $G_p = k_B T \rho / N_e$ .<sup>10</sup>

The entanglement time in the lattice model is determined in the following manner. We take mean-square displacement (msd) data for the middle monomer (mm) for the highest value of  $Z$  (i.e.,  $Z = 25.6$ , corresponding to  $N = 5120$ ), as it shows a clean  $t^{1/4}$  regime for about 2 decades. In the pre-entangled time regime the msd data behave as  $t^{0.44}$ . (Although a single chain in this model behaves purely as a SAW Rouse chain,<sup>40</sup> in the pre-entangled melt the tagged chain exhibits consistent deviations from the Rouse behavior. This will be dealt with in more detail in a future publication on unentangled melts,<sup>63</sup> as well as in section IIID.) Using these exponents the crossover point is identified in Figure 5, yielding the entanglement time  $\tau_e \approx 32\,694$  ( $\log \tau_e \approx 4.5$ ).

**C. Generation and Analysis of  $C(t)$  from Simulations and Estimation of Parameters Characterizing the Regimes I and II.** Experimentally, the OACF is based on the orientations of a single bond in the chains. In order to maintain consistency, one should also obtain the OACF from single bond orientations in the simulations, and a bond close to the middle of the chains should suffice for this purpose. To be supremely consistent, one could choose the orientation of the unit vector

$$\hat{u}_1(t) = \frac{\tilde{\mathbf{r}}_{N/2+1}(t) - \tilde{\mathbf{r}}_{N/2-1}(t)}{|\tilde{\mathbf{r}}_{N/2+1}(t) - \tilde{\mathbf{r}}_{N/2-1}(t)|} \quad (4)$$

where  $\tilde{\mathbf{r}}_{N/2\pm 1}(t) = [\mathbf{r}_{N/2}(t) + \mathbf{r}_{N/2\pm 1}(t)]/2$ . For the above, for a chain of length  $N$ , we number the monomers 0, 1, ...,  $N$  from

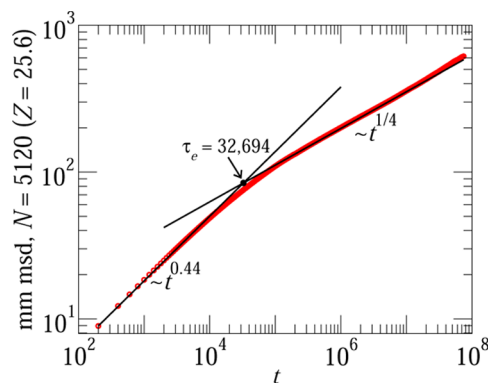


**Figure 5.** Determination of the entanglement time  $\tau_e$  from the middle monomer (mm) mean-square displacement (msd) simulation data for  $N = 5120$  ( $Z = 25.6$ ). The data exhibit clean  $t^{1/4}$  regime for about two decades ( $2 \times 10^5 \lesssim t \lesssim 2 \times 10^7$ ). The pre-entangled regime exhibits an anomalous exponent  $\approx 0.44$ . The intersection point of these two power laws (denoted by black lines) passing through the simulation data (open red circles) is identified to be the entanglement time  $\tau_e \approx 32\,694$  for simulations.

one end to the other and note their locations at time  $t$  as  $\mathbf{r}_0(t)$ ,  $\mathbf{r}_1(t)$ , ...,  $\mathbf{r}_N(t)$ . However, since there are 12 lattice directions from every site in the simulations, the spatial configuration of a chain at the monomeric level in the simulation model is imaginably quite jagged. This jagged nature manifests itself by high level of noise in the OACF data obtained from  $\hat{u}_1(t)$ .

In order to achieve higher signal-to-noise ratio for the OACF in simulations, we define

$$\tilde{\mathbf{r}}_{N/2\pm s}(t) = \frac{1}{s+1} [\mathbf{r}_{N/2}(t) + \mathbf{r}_{N/2\pm 1}(t) + \dots + \mathbf{r}_{N/2\pm s}(t)] \quad (5)$$

and subsequently consider the unit vector

$$\hat{u}_s(t) = \frac{\tilde{\mathbf{r}}_{N/2+s}(t) - \tilde{\mathbf{r}}_{N/2-s}(t)}{|\tilde{\mathbf{r}}_{N/2+s}(t) - \tilde{\mathbf{r}}_{N/2-s}(t)|} \quad (6)$$

which subtends an angle  $\theta_s^{(z)}(t)$  to the  $z$ -axis, and define

$$C_s^{(z)}(t) = 5 \langle P_2[\theta_s^{(z)}(t + \tau)] P_2[\theta_s^{(z)}(\tau)] \rangle_{t, \text{ens}} \quad (7)$$

as in eq 1. In fact, since the systems in simulations are isotropic, in order to improve statistics, we also consider the angles  $\theta_s^{(x)}(t)$  and  $\theta_s^{(y)}(t)$  that the unit vector  $\hat{u}_s(t)$  subtends with the  $x$ - and the  $y$ -axis, respectively, and define

$$C_s(t) = \frac{5}{3} [C_s^{(x)}(t) + C_s^{(y)}(t) + C_s^{(z)}(t)] \quad (8)$$

as a proxy to the experimental quantity  $C(t)$ .

In Figure 6a we plot the  $C_s(t)$  data for  $N = 3600$  ( $Z = 18$ ) for different values of  $s$ . The plots clearly confirm the anticipation that choosing a lower value of  $s$  implies more noise in the data. More importantly, the plots also confirm that beyond the entanglement time the curves run parallel to each other for different values of  $s$ ; i.e., for  $t > \tau_e$  the choice of the  $s$ -value only determines the amplitude. This is as such not surprising; at long times, the local relaxation of the OACF is coupled to the global relaxation behavior of the chains, so the  $C_s(t)$  curves ought to run parallel to each other at long times as long as the condition  $s \ll N$  is satisfied. Given this confirmation, the fits and explicit comparisons in regimes II and beyond (addressed in more detail below) we have used  $s = 7$  data in Figure 4. The choice is



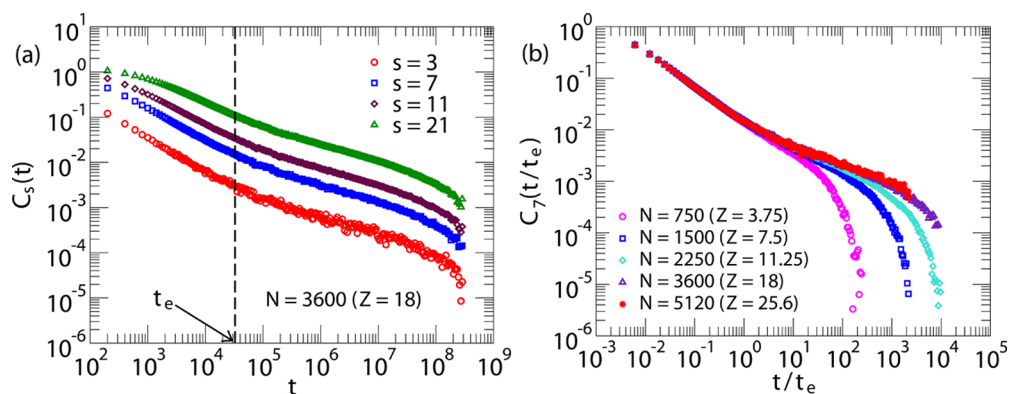


**Figure 6.**  $C_s(t)$  data normalized to  $C_s(0)$  (a) for  $N = 3600$  ( $Z = 18$ ) and  $s = 3, 7, 11$ , and  $21$  as well as (b) for  $s = 7$  and  $N = 750, 1500, 2250, 3600, 5120$  ( $Z = 3.75, 7.5, 11.25, 18, 25.6$ ) with scaled time axis. The plots in (a) confirm that beyond the entanglement time the curves run parallel to each other for different values of  $s$ .

motivated by the fact that we would like to determine the behavior of  $C_s(t)$  as localized as possible within the chain without succumbing to the noise in the data.

The  $C_7(t)$  plotted in Figure 6b for the different chain lengths exhibit a reassuring resemblance to the experimental OACFs in Figures 3 and 4a as well as to our previously published data,<sup>25,26</sup> where regime I data as obtained from  $^1\text{H}$   $T_1$  NMR relaxometry<sup>24</sup> were added to complement the dynamics at shorter time scales, i.e., in regime I. For more quantitative comparisons between simulated and experimental data, we rely on fitting procedures, as follows, characterizing in detail the functional shape of the  $C(t)$ .

The analysis procedures of the so-obtained  $C_s(t)$  are demonstrated in Figure 7 on two examples,  $s = 3$  and  $7$ , for  $N = 2250$  ( $Z = 11.25$ ). All analyses were performed in

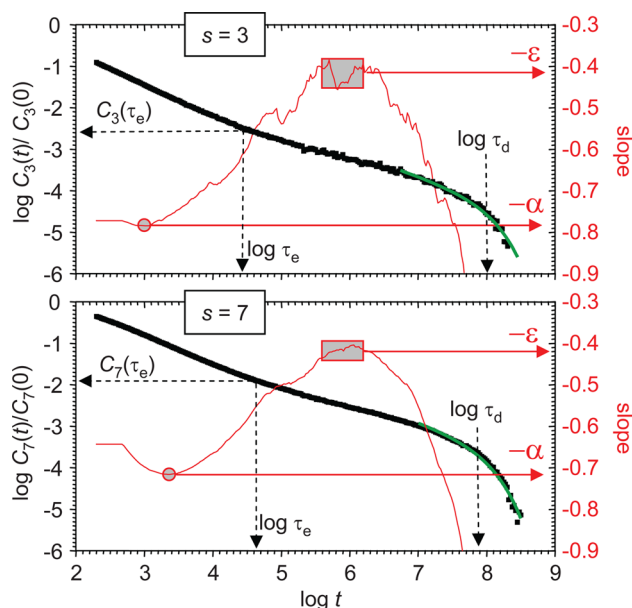


**Figure 7.** Analysis of  $C_3(t)$  and  $C_7(t)$  for  $N = 2250$  ( $Z = 11.25$ ). Power-law exponents for regimes I and II representing the steepest slopes,  $\alpha$  and  $\varepsilon$ , respectively, are determined by a derivative analysis (thin solid line, right y scale). Because of larger noise, the latter is obtained as an average over a half-decade interval in time. Apparent regime transition times  $\tau_{e,d}$  are then estimated from the first kink and by a fit (thick solid line) to the data in logarithmic units, as described in the text.

logarithmic units of the normalized  $C_s(t)$  and time. In order to characterize the functions in regimes I and II of the tube model, where power laws are predicted,<sup>24,25,32</sup> we used a derivative analysis, involving a polynomial fit of second order to 30 adjacent data points and evaluating the slope at its center. It is observed (solid thin curves in Figure 7) that regime I is characterized by a rather smooth curvature (variable slope), while in regime II the data vary only weakly over a larger interval of  $1/2$  to  $1$  decade in time but is more noisy. The apparent exponents in these two regimes are identified by the extrema of the thin curves. The value of  $\alpha$ , the apparent exponent in regime I, is read off directly from the local minimum, while  $\varepsilon$  and its error were taken as the average and standard deviation, respectively, over a half-decade interval around the maximum of the solid thin curves.

Then, an apparent  $\tau_e$  and the corresponding amplitude  $C_s(\tau_e)$  are estimated from the “kink”, identified as the point where the slope of the solid thin curves in Figure 7 equals about the average of  $\alpha$  and  $\varepsilon$ . The disentanglement time  $\tau_d$  is finally identified by fitting the tail end of the  $C_s(t)$  data to the analytical result for regime III/IV motion.<sup>25,32</sup>

Since the shape of the  $C_s(t)$  in regime I is strongly dependent on the coarse-graining variable  $s$ , we have also evaluated the simulation data for  $s = 1$ , further testing a shorter time step  $\Delta t$ . Figure 8 demonstrates that the magnitude of  $C_1(t)$  is indeed much lower in regime I and that the shorter  $\Delta t = 10$  data is identical to the  $\Delta t = 200$  data but extends to shorter times.

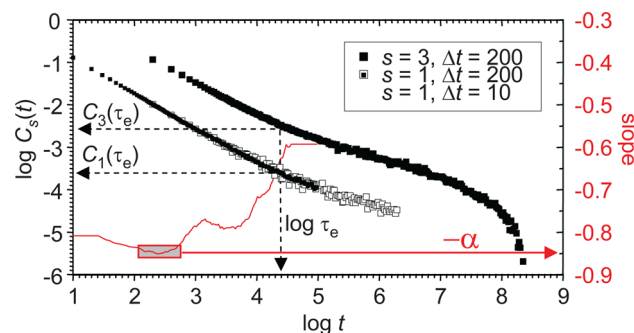


**Figure 8.** Comparison of  $C_1(t)$  and  $C_3(t)$  for  $N = 2250$  ( $Z = 11.25$ ), with the former extracted on the basis of a longer and a shorter time step. The solid line on the right scale shows the derivative of the  $\Delta t = 10$  data. Less coarse graining and higher time resolution are needed to extract meaningful values for the regime I slope  $\alpha$  and  $C(\tau_e)$ .

Consequently, we have performed a derivative analysis on the  $\Delta t = 10$  data, now revealing larger interval of near-constant power law exponent  $-\alpha$  that varies by less than 0.1 over 2 decades in time. An average over the half-decade interval about its minimum yields  $\alpha \approx 0.83 \pm 0.01$ .

The values of  $\alpha$ ,  $\tau_e$ , and  $\varepsilon$  that characterize regimes I and II are plotted as a function of  $s$  and as a function of  $N$  in Figures 9 and 10a, respectively. They show the expected trends, i.e.,  $\tau_e$  (Figure 9) and  $\varepsilon$  (Figure 10a), have little or no dependence on  $s$  (for  $\varepsilon$  the smoothing affects only the error intervals, but not the actual average values), while  $\alpha$  decreases and  $C_s(t = \tau_e)$  increases, both clearly nonlinearly, with increasing  $s$ . This is only to be expected; upon smoothing over longer length scales the dynamical variations over increasing length and time scales simply get lost.

**D. Comparison of Simulation Results with Experiments.** Tube theory in regime I, i.e., simply the Rouse theory, predicts that we should expect an exponent  $-1$  for the decay of  $C(t)$ , yet  $\alpha$  extrapolates to  $\approx -0.83$  (Figure 9). This is close to an experimental value of the order of  $-0.85$  that is obtained from  $T_1$  relaxometry data.<sup>24</sup> The investigation of the quantity  $\alpha$  is deferred to a separate publication on unentangled melts<sup>63</sup> using Rouse mode analysis on the same simulation model: the analysis reveals that the exponent  $\alpha$  is a true exponent and has been found to be in the range  $0.8$ – $0.85$  in many simulations and experiments. (One of its consequences is that in regime I the mean-square displacement of a tagged monomer is seen to increase in time as  $t^{0.44}$ , which is shown in Figure 5.)

Reassuringly, the weakly varying  $\log \tau_e$  extrapolates to the value  $\log \tau_e \approx 4.4$ , also identified by the msd analysis (Figure 5). The position of the kink at  $C_s(\tau_e)$  (Figure 7) is seen to move to higher values in both amplitude and time upon smoothing. The  $s = 1$  limiting value  $C_1(\tau_e) \approx S_e^2 \approx 0.00022$  is appreciably lower than what is found for higher  $s$  and should be characteristic for the number of entangled segments  $N_e$  in the simulated chains.  $N_e$  is estimated to  $3/(5 \times 0.015) \approx 40$ .<sup>25,26</sup> This is only in qualitative agreement with the “rheological” determination of  $N_e$  ( $= 200 \pm 20$ ). Noting that the  $s = 1$  case describes orientation fluctuations of two combined lattice monomers, the above estimate suggests that the effective statistical segment in the simulation corresponds to around one

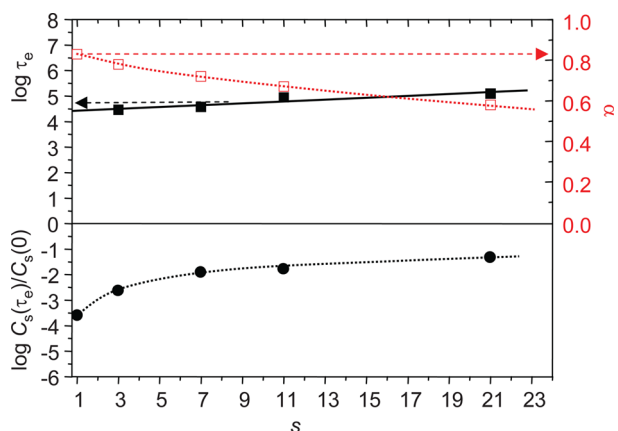


**Figure 9.** Results of the chain-length-independent fit parameters to the  $C_s(t)$  in Figures 7 and 8 as a function of the smoothing variable  $s$ . The values are averages over all chain length. The solid line represents a linear fit to  $\log \tau_e$  and the dotted lines just guide the eye for the visibly nonlinear relationships.

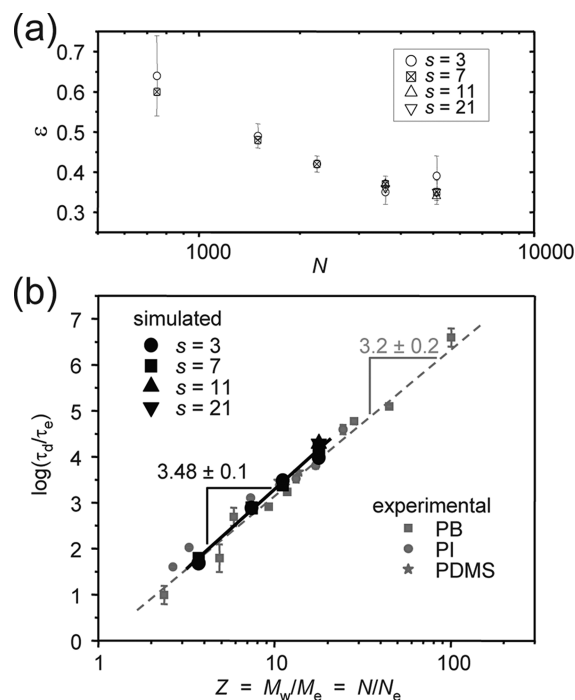


**Figure 10.** Results of the chain-length-dependent fit parameters to the  $C_s(t)$  in Figure 7. (a) Regime II exponent  $\varepsilon$  as a function of chain length and (b) normalized terminal time vs the number of entangled strands  $Z$ , as compared to previous experimental results for three different polymers<sup>26</sup> shown in gray.

rather than two lattice monomers, and is likely affected by the simulation lattice.

With the two key parameters  $N_e$  and  $\tau_e$  identified (section IIIB), we are now in a position to meaningfully compare the chain-length-dependent fit results from the  $C_s(t)$  (previous section) with those from experiments, as they can be expected to be universal. In this way, we seek to validate the results of our coarse-grained simulations.

Figure 10a shows the  $N$ -dependent results for the regime II slope  $\varepsilon$  for the different values of  $s$ . The  $\varepsilon$  values for  $s = 7$  are confronted with the already discussed experimental results in Figure 4. Considering potential systematic errors in the definitions of the experimental  $M_e$  vs the simulated  $N_e$ , the agreement is very good indeed, in particular with the clean tagged-chain results taken from  $^2\text{H}$  NMR. We note again that the values from  $T_1$  relaxometry are subject to potential systematic overestimation. We take the good fit to the reliable tagged-chain experimental data as the strongest evidence for the validity of our simulation results, as the chain-length dependence of  $\varepsilon$  is a subtle and unexpected effect related to CR processes.<sup>25,33</sup>

A comparison of the scaled terminal times  $\tau_d$  from the simulations are compared to previously published data for three different flexible homopolymers<sup>26</sup> in Figure 10b. The results match almost perfectly, with a linear fit in the log–log representation, confirming  $\tau_d = \tau_e$  at  $N/N_e = 1$ . The scaling exponent is within the errors, further in perfect agreement with the well-known value  $m_\eta \approx 3.4 \pm 0.2$  from rheology.

## IV. CONCLUSIONS

Our study has demonstrated, first, that pure tagged-chain rotational dynamics can be probed by isotope-dilution  $^1\text{H}$  as well as  $^2\text{H}$  MQ NMR and, second, that these results are in



quantitative agreement with results from a novel lattice model capable of reflecting the dynamics of entangled chains over more than 10 decades in scaled time.

Specifically, it was shown that  $C(t)$  determined by  $^1\text{H}$  MQ NMR in the present variant, constructing it from the short-time response relying on time–temperature superposition, is even for protonated bulk samples only weakly (yet systematically) affected by interchain dipolar couplings. The response is dominated by intrasegmental couplings reflecting tagged-chain dynamics. The latter can be probed selectively by the mentioned isotope-dilution  $^1\text{H}$  as well as  $^2\text{H}$  experiments, where the former have indicated that the main effect of interchain couplings in fully protonated systems is an increase of the apparent amplitude of the segmental orientation correlation function (OACF) by about a factor of 2, corresponding to an apparent increase of the local segmental order parameter by only a factor of 1.4.

The apparent power-law exponent of the segmental OACF describing regime II dynamics of the tube model, whose chain-length dependence was previously shown to reflect subtle constraint-release effects on the tube constraint, was shown to be overestimated only slightly in protonated bulk samples, in strong contrast to previous  $^1\text{H}$   $T_1$  NMR relaxometry results, which are dominated by interchain couplings and translational motion. Tagged-chain rotational dynamics appears more difficult to be probed by this latter technique due to the different measurement concept.

The simulation results from a novel lattice model were shown to faithfully reflect entangled dynamics in terms of a clear regime transition of the segmental mean-square displacement at the entanglement time  $\tau_e$  and allow for an extraction of the number of lattice monomers  $N_e$  in an entangled unit. These parameters can be used to probe universal features of the chain dynamics at larger scaled times. The segmental OACF was extracted from the simulation data, and the impact of a smoothing procedure was discussed.

Smoothing was shown to not affect the universal features of the chain dynamics, and a near-perfect agreement with the experimental NMR results was found. This stresses the validity and the use of the novel simulation method to probe deviations from tube-model predictions and variants thereof and to possibly identify their microscopic origin.

## ■ APPENDIX A. ISOTOPE EFFECTS AND TIME–TEMPERATURE SUPERPOSITION

A recent isotope dilution study indicated weak but significant isotope effects on the segmental correlation time  $\tau_s(T)$  of PB as probed by field-cycling  $^1\text{H}$  relaxometry.<sup>28,29</sup> In the protonated PB bulk,  $\tau_s(T)$  as probed by  $^1\text{H}$  NMR relaxometry<sup>22</sup> and dielectric spectroscopy<sup>64</sup> agree reasonably well and can be described by the usual Vogel–Fulcher (VF) law and are further consistent with the segmental relaxation time as calculated<sup>21,26</sup> from the monomeric friction coefficient determined by rheology.<sup>51</sup>

Now, MQ NMR, owing to its limited time range,<sup>21,25,26,38</sup> relies on using a given  $\tau_s(T)$  (or alternatively,  $\tau_e = \tau_s N_e^2$ ) for time–temperature superposition (TTS). Therefore, potential isotope effects on  $\tau_s(T)$  should be taken into account, as they affect the shape of the segmental OACF,  $C(t)$ , as constructed from the data. In the following, we summarize rheology results that prove the actual absence of an isotope effect on the VF parameters and present a discussion of the VF parameters used for time–temperature superposition.

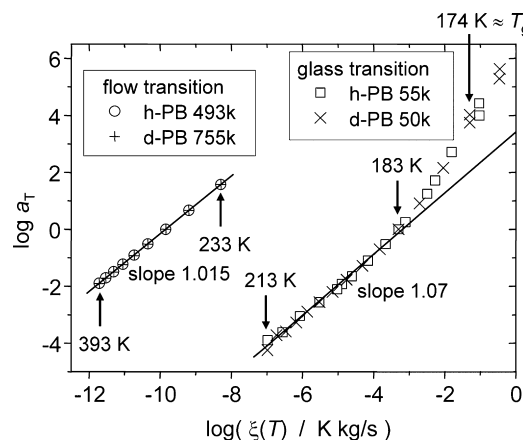


**Figure 11.** Comparison of logarithmic shift factors from shear rheology with calculated values of the logarithmic monomeric friction coefficient using the parameters from ref 51; see below eq 3 for values. The data reveal near-perfect proportionality in the higher temperature range. Note that the upturn of the glass-transition-based data toward larger friction coefficients (lower temperatures) does *not* indicate the  $T_g$ -related slowdown but rather the deviation from the VF relation determined in the flow transition region.

### 1. Rheological Investigation of Potential Isotope Effects

Mechanical spectroscopy in shear geometry, using an Ares G2 rheometer with a plate–plate geometry (8 mm diameter,  $\sim 1$  mm gap), has been performed on two hydrogenated and two deuterated PB samples following standard procedures. Results for the shift factors  $a_T$  ( $\propto \xi(T) \propto \tau_s(T) \times T$ ) needed to construct master curves for the complex shear modulus (not shown) are collected in Figure 11. For the lower- $M_w$  samples, the reference temperature was 183 K, and the data reflect the master curve construction in the range of the glass transition (segmental dynamics). In this case, in order to avoid problems with the stiffness of the sample,<sup>65</sup> the plate–plate distance was increased, drawing a melt filament. This complicates the accurate determination of absolute values for the modulus but does not compromise the determination of  $a_T$  values. For the higher- $M_w$  samples, the reference temperature was 273 K, focusing on the flow transition ( $a_T \propto \tau_d(T) \times T$ ). It is seen that the shift factors of hydrogenated and deuterated samples are in both cases identical within the very small experimental error. Thus, there is no indication for an isotope effect on  $\tau_s$ , identifying the finding of Rössler and co-workers<sup>28</sup> as a weak “NMR effect”.

Figure 11 also demonstrates that the shift factors determined for the different regimes do not follow the same VF relation. It is thus important to use VF parameters for TTS that have been calibrated in a similar temperature range. This is the case for the data of Monnerie and co-workers<sup>51</sup> that we rely upon. The near-perfect proportionality of our newly measured high-temperature shift factors and friction coefficient data from this reference also prove that  $T_{VF} \approx 126$  K holds well for the samples studied herein.

As to the possible origin of the apparent isotope effect in  $T_1$  NMR (see the circles in Figure 12), we find that in ref 29 it is explicitly noted that the maximum of the “NMR susceptibility” as the quantity subject to TTS, which leads to the  $\tau_s(T)$  determined by  $T_1$  NMR, is a weak function of temperature for different polymers. Similar findings have been reported for certain small-molecule liquids.<sup>35</sup> Such a dependence invalidates TTS to a certain degree, as discussed in the same reference, and

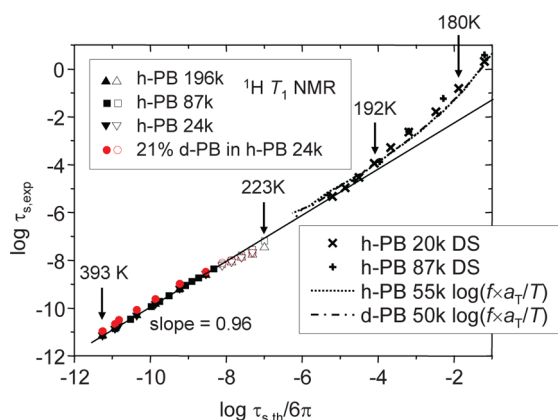


**Figure 12.** Log–log correlation of experimental  $\tau_s(T)$  from  $^1\text{H}$   $T_1$  NMR relaxometry<sup>22,28,29</sup> and dielectric spectroscopy (DS)<sup>64</sup> with a rescaled  $\tau_s(T)$  calculated by eq 3. The solid line is a linear fit of the bulk  $^1\text{H}$   $T_1$ -based data in the higher temperature range (solid symbols), which is most reliable due to the observed maximum in the NMR susceptibility. The open symbols denote the less reliable range. Dotted and dash-dotted lines interpolate our low-temperature rheology data for  $a_T$  (Figure 11) divided by  $T$  and scaled by a suitable factor  $f$ .

may originate from a change in average proton–proton distances as a function of temperature, i.e., changes in the density<sup>29</sup> or the conformer mixture. Such changes may be different for the inter- and intrachain contributions to  $T_1$ ,<sup>28</sup> which means that isotope dilution would trivially affect the results of TTS when the shifted data reflect two independent processes with slightly different temperature dependence.

## 2. Discussion of Parameters Used for Time–Temperature Superposition

As the  $C(t)$  construction relies on representative values for  $\tau_s(T)$ , we here present a comparison of the literature-based relation  $\tau_s(T) = \tau_e(T)/N_e^2$ , eq 3, that we use for master curve construction with alternative measures, such as the values derived from field-cycling  $T_1$  relaxometry<sup>22,28,29</sup> and dielectric spectroscopy (DS).<sup>64</sup> Here, it is important to again stress that deviations between values measured with different techniques, and deviations from a common VF relation that is calibrated for a narrow temperature range, are rather common (see Figure 11). The 200–400 K range of interest corresponds to  $\tau_s(T)$  of the order of  $10^{-6}$ – $10^{-12}$  s, which is marginally covered by very-high-frequency dielectric spectroscopy (DS) or very well by field-cycling  $T_1$  relaxometry as well as rheological data when focusing on the flow transition.

Figure 12 presents a correlation of  $\tau_s(T)$  calculated by eq 3 with the data of Rössler and co-workers.<sup>22,28</sup> We have now divided  $\tau_s(T)$  from eq 3 by another factor of  $6\pi$ , which, probably coincidentally, provides values that are almost identical to the experimental data. This may well be a coincidence, yet it is notable that the effective “fudge factor”  $\kappa = 6\pi^2$  in eq 3 now coincides with the value given in some presentations of Rouse theory. More importantly, we observe a log–log slope near unity, corresponding to near-perfect proportionality. We note that the effect of the explicit temperature prefactor in eq 3 is almost negligible, as the temperature dependence of the friction coefficient dominates. We also plot one data set obtained by isotopic dilution to 21% (circles), which gives higher apparent  $\tau_s$  and a slightly reduced slope.

The data from DS cover the lower temperature range from above to around  $T_g$ , and deviate again characteristically from the high-temperature data. The deviation is in fact the same as the one observed in Fig. 11, as proven by the interpolated rheology data matched to the DS data with a common factor  $f$ , including the division by  $T$  as required by eq 3. It is noted that DS measures a different correlation function than NMR, which amounts to a factor of 3 difference in  $\tau_s$  for the simple model case of rotational diffusion. This deviation is however hardly perceptible in the plot. In all, we can conclude that the published microscopic measures of  $\tau_s$  are, apart from a constant factor, in very good agreement with predictions based upon the monomeric friction coefficient from rheology. The apparently prolonged  $\tau_s$  measured for isotopically dilute samples in the high-temperature range deviate only weakly but systematically, corresponding to a slightly modified VF relation.

In this context, the isotope effect is seen to be rather small and cannot be held responsible for significant systematic errors and the deviations between the different NMR techniques, as discussed in the context of Figure 4b. This conclusion is supported by evaluating in how far results for the regime II exponent  $\varepsilon$  change when we explicitly use, e.g., interpolated  $\tau_s(T)$  values based upon Rössler’s  $T_1$ -based data for protonated or isotopically dilute samples<sup>28</sup> as the basis of TTS. We then found  $\varepsilon$  values that were only higher by about 0.01–0.03 than the reported values, which is almost within the error interval of our derivative analysis and way beyond the deviations from the  $\varepsilon$  values that were estimated from the  $T_1$  data directly (see Figure 4). We further found similar systematic changes when varying the  $T_{VF}$  by a few K, accounting for possible uncertainties in the microstructure of the samples, leading to slight differences in  $T_g$  (see the Materials and Methods section). We conclude that the used TTS procedure based upon eq 3 is rather robust and that uncertainties related to it cannot explain the significant deviations of our data from simple tube-model predictions and their use in understanding these.

## ■ APPENDIX B. TIME SCALING EXPONENTS FROM $T_1$ NMR RELAXOMETRY

Noting the systematic deviations of the regime II time-scaling exponents  $\varepsilon$  between time-domain MQ NMR and  $T_1$  NMR relaxometry, we address the potential origin of such deviations by help of model analyses of metadata. Figure 13a shows  $C(t)$  according to the analytical approximation based upon the tube model<sup>32,38</sup> with parameters derived from our experimental data.<sup>26</sup> The data for the three different chain lengths exhibit the clean power-law regions expected for regimes I and II with exponents  $\alpha$  and  $\varepsilon$ , respectively, while the combined regime III/IV formula by Ball et al.<sup>32</sup> predicts a slope of  $-0.5$  only at the beginning of regime III.

In Figure 13b, we plot predictions for the frequency-dependent NMR susceptibility,<sup>22</sup> which is calculated as  $\nu/T_1(\nu) \sim \nu(J(\nu) + 4J(2\nu))$ . Here, the spectral density  $J(\nu)$  is calculated as numerical Fourier transform of  $C(t)$  on an evenly spaced logarithmic scale, using an algorithm described by Blochowicz.<sup>66</sup> A derivative analysis immediately reveals that there is no simple relation between time power-law exponents of  $C(t)$  and frequency power-law exponents of the NMR susceptibility. The slope in log–log units of frequency varies continuously, and only for regime I the input exponent of  $-0.85$  is recovered as positive value in a small frequency range for the highest chain

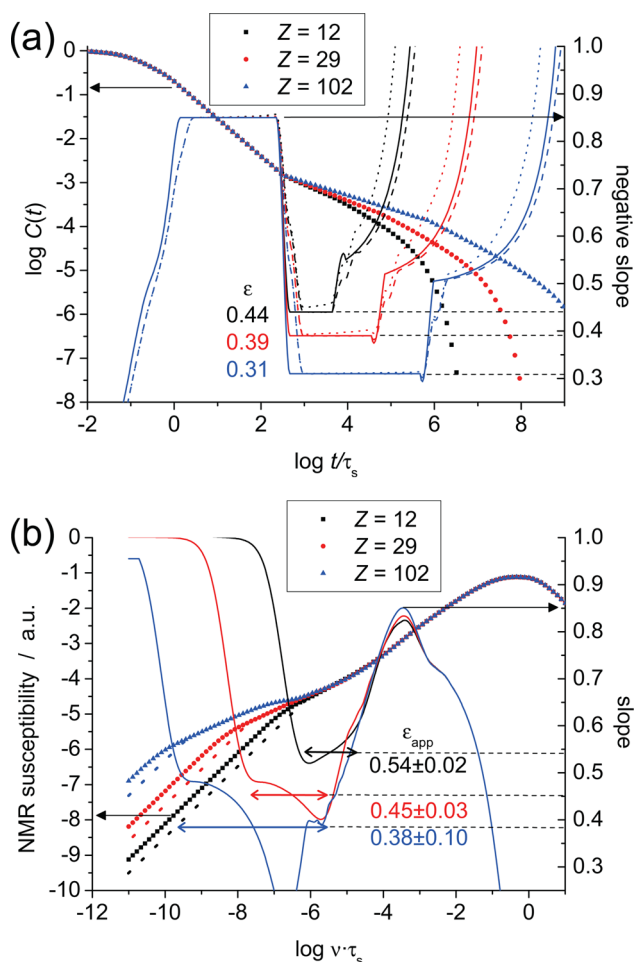


**Figure 13.** (a) Analytical approximations of  $C(t)$ <sup>38</sup> representative for PB 24k ( $Z = 12$ ), 55k ( $Z = 29$ ), and 196k ( $Z = 102$ ), using the parameters published in ref 26. (b) NMR susceptibility,  $\sim \nu/T_1(\nu)$ , calculated from the Fourier-transformed  $C(t)$ . The thick dotted lines indicate analytical continuations to low frequencies that are shifted by half a decade. The thin lines in both plots (right y scales) represent the slopes obtained by numerical derivative analysis. In (a) this includes analyses of back-transformed  $1/T_1(\nu)$  (dashed) and of the analytically continued  $1/T_1(\nu)$  with shifted low-frequency branch (dotted).

length. This highlights the danger inherent to linearly fitting larger frequency intervals.

Rössler and co-workers fitted larger frequency or time intervals to extract  $\epsilon$ . Tentatively fitting the frequency range covering regimes II and III in which the slope is lowest (corresponding to averaging the slope values), we obtain the apparent  $\epsilon$  values given in the legend of Figure 13b. The error intervals indicate the standard deviation over the fitted ranges indicated by the double arrows. Comparing this with the input values shown in (a), we consistently note an overestimation of  $\epsilon$  by about 0.1.

A more robust alternative for the estimation of  $\epsilon$  from the  $T_1$  data is a back-transformation to obtain an approximate  $C(t)$ . This involves the assumption that  $J(\nu) = J(2\nu)$  and requires an analytical continuation of  $\nu/T_1(\nu)$  to zero frequency with a power law  $\sim \nu^1$  due to the limited experimental  $\nu$  range. This may be ambiguous if the terminal range is not reached in actual experiments. The influence of both issues was tested. Figure 13a also shows derivative analyses (thin lines) of so-obtained  $C(t)$ , where the dashed line is a direct back transformation of

$1/T_1(\nu)$  showing the weak influence of the  $J(\nu) = J(2\nu)$  approximation, and the dotted line is from data where the terminal regime were willfully shifted to higher frequencies by half a decade. Both issues do not appear to seriously affect a determination of  $\epsilon$  from  $C(t)$  if the fits are restricted to regime II. Tentatively fitting a larger range, i.e., including half of regime III (before the visually clear onset of the influence of terminal dynamics), also leads to an overestimation of  $\epsilon$  by about 0.1.

## AUTHOR INFORMATION

### Corresponding Authors

\*E-mail kay.saalwaechter@physik.uni-halle.de (K.S.).

\*E-mail D.Panja@uu.nl (D.P.).

### Notes

The authors declare no competing financial interest.

## ACKNOWLEDGMENTS

Funding was provided by the Deutsche Forschungsgemeinschaft (DFG SA982/4-2). We are indebted to Nail Fatkullin, Ernst Rössler, Axel Herrmann, and Marius Hofmann for many fruitful discussions, comments, and the latter three for providing their raw data.

## REFERENCES

- (1) Lodge, T. P. Reconciliation of the Molecular Weight Dependence of Diffusion and Viscosity in Entangled Polymers. *Phys. Rev. Lett.* **1999**, *83*, 3218–3221.
- (2) Abdel-Goad, M.; Pyckhout-Hintzen, W.; Kahle, S.; Allgaier, J.; Richter, D.; Fetters, L. J. Rheological Properties of 1,4-Polyisoprene over a Large Molecular Weight Range. *Macromolecules* **2004**, *37*, 8135–8144.
- (3) Ferry, J. D. *Viscoelastic Properties of Polymers*; John Wiley & Sons Ltd.: New York, 1980.
- (4) Edwards, S. F. The Statistical Mechanics of Polymerized Material. *Proc. Phys. Soc.* **1967**, *92*, 9–16.
- (5) de Gennes, P. G. Reptation of a Polymer Chain in the Presence of Fixed Obstacles. *J. Chem. Phys.* **1971**, *55*, 572–579.
- (6) de Gennes, P. G. *Scaling Concepts in Polymer Physics*; Cornell University Press: Ithaca, NY, 1979.
- (7) Doi, M.; Edwards, S. F. Dynamics of Concentrated Polymer Systems. Part 1. Brownian Motion in the Equilibrium State. *J. Chem. Soc., Faraday Trans. 2* **1978**, *74*, 1789–1801.
- (8) Doi, M.; Edwards, S. F. Dynamics of Concentrated Polymer Systems. Part 2. Molecular Motion under Flow. *J. Chem. Soc., Faraday Trans. 2* **1978**, *74*, 1802–1817.
- (9) Doi, M.; Edwards, S. F. Dynamics of Concentrated Polymer Systems. Part 3. The Constitutive Equation. *J. Chem. Soc., Faraday Trans. 2* **1978**, *74*, 1818–1832.
- (10) Doi, M.; Edwards, S. F. *The Theory of Polymer Dynamics*; Clarendon Press: Oxford, 1986.
- (11) Milner, S. T.; McLeish, T. C. B. Reptation and Contour-Length Fluctuations in Melts of Linear Polymers. *Phys. Rev. Lett.* **1998**, *81*, 725–728.
- (12) Likhtman, A. E.; McLeish, T. C. B. Quantitative Theory for Linear Dynamics of Linear Entangled Polymers. *Macromolecules* **2002**, *35*, 6332–6343.
- (13) McLeish, T. C. B. Tube Theory of Entangled Polymer Dynamics. *Adv. Phys.* **2002**, *51*, 1379–1527.
- (14) Liu, C.-Y.; Keunings, R.; Bailly, C. Do Deviations from Reptation Scaling of Entanglement Polymer Melts Result from Single- or Many-Chain Effects? *Phys. Rev. Lett.* **2006**, *97*, 246001.
- (15) Read, D. J.; Jagannathan, K.; Likhtman, A. E. Entangled Polymers: Constraint Release, Mean Paths, and Tube Bending Energy. *Macromolecules* **2008**, *41*, 6843–6853.
- (16) Adachi, K.; Wada, T.; Kawamoto, T.; Kotaka, T. Dielectric Spectroscopy on Dilute Blends of Polyisoprene/Polybutadiene: Effects



of Matrix Polybutadiene on the Dynamics of Probe Polyisoprene. *Macromolecules* **1995**, *28*, 3588–3596.

(17) Matsumiya, K.; Kumazawa, K.; Nagao, M.; Urakawa, O.; Watanabe, H. Dielectric Relaxation of Monodisperse Linear Polyisoprene: Contribution of Constraint Release. *Macromolecules* **2013**, *46*, 6067–6080.

(18) Zamponi, M.; Monkenbusch, M.; Willner, L.; Wischnewski, A.; Farago, B.; Richter, D. Contour Length Fluctuations in Polymer Melts: A Direct Molecular Proof. *Europhys. Lett.* **2005**, *72*, 1039–1044.

(19) Zamponi, M.; Wischnewski, A.; Monkenbusch, M.; Willner, L.; Richter, D.; Likhtman, A. E.; Kali, G.; Farago, B. Molecular Observation of Constraint Release in Polymer Melts. *Phys. Rev. Lett.* **2006**, *96*, 238302.

(20) Pearson, D. S.; Fetters, L. J.; Graessley, W. W.; Ver Strate, G.; von Meerwall, E. Viscosity and Self-Diffusion Coefficient of Hydrogenated Polybutadiene. *Macromolecules* **1994**, *27*, 711–719.

(21) Graf, R.; Heuer, A.; Spiess, H. W. Chain-Order Effects in Polymer Melts Probed by  $^1\text{H}$  Double-Quantum NMR Spectroscopy. *Phys. Rev. Lett.* **1998**, *80*, 5738–5741.

(22) Kariyo, S.; Gainaru, C.; Schick, H.; Brodin, A.; Novikov, V. N.; Rössler, E. A. From a Simple Liquid to a Polymer Melt: NMR Relaxometry Study of Polybutadiene. *Phys. Rev. Lett.* **2006**, *97*, 207803.

(23) Kehr, M.; Fatkullin, N.; Kimmich, R. Deuteron and Proton Spin-Lattice Relaxation Dispersion of Polymer Melts: Intrasegment, Intrachain, and Interchain Contributions. *J. Chem. Phys.* **2007**, *127*, 084911.

(24) Herrmann, A.; Novikov, V. N.; Rössler, E. A. Dipolar and Bond Vector Correlation Function of Linear Polymers Revealed by Field Cycling  $^1\text{H}$  NMR: Crossover from Rouse to Entanglement Regime. *Macromolecules* **2009**, *42*, 2063–2068.

(25) Vaca Chávez, F.; Saalwächter, K. NMR Observation of Entangled Polymer Dynamics: Tube Model Predictions and Constraint Release. *Phys. Rev. Lett.* **2010**, *104*, 198305.

(26) Vaca Chávez, F.; Saalwächter, K. Time-Domain NMR Observation of Entangled Polymer Dynamics: Universal Behavior of Flexible Homopolymers and Applicability of the Tube Model. *Macromolecules* **2011**, *44*, 1549–1559.

(27) Herrmann, A.; Kresse, B.; Gmeiner, J.; Privalov, A. F.; Kruk, D.; Fujara, F.; Rössler, E. A. Protracted Crossover to Reptation Dynamics: A Field Cycling  $^1\text{H}$  NMR Study Including Extremely Low Frequencies. *Macromolecules* **2012**, *45*, 1408–1416.

(28) Herrmann, A.; Kresse, B.; Wohlfahrt, M.; Bauer, I.; Privalov, A. F.; Kruk, D.; Fatkullin, N.; Fujara, F.; Rössler, E. A. Mean Square Displacements and Reorientational Correlation Function in Entangled Polymer Melts Revealed by Field Cycling  $^1\text{H}$  and  $^2\text{H}$  NMR Relaxometry. *Macromolecules* **2012**, *45*, 6516–6526.

(29) Hofmann, M.; Herrmann, A.; Abou Elfadl, A.; Kruk, D.; Wohlfahrt, M.; Rössler, E. A. Glassy, Rouse, and Entanglement Dynamics As Revealed by Field Cycling  $^1\text{H}$  NMR Relaxometry. *Macromolecules* **2012**, *45*, 2390–2401.

(30) Meier, R.; Herrmann, A.; Kresse, B.; Privalov, A. F.; Kruk, D.; Fujara, F.; Rössler, E. A. Long-Time Diffusion in Polymer Melts Revealed by  $^1\text{H}$  NMR Relaxometry. *ACS Macro Lett.* **2013**, *2*, 96–99.

(31) Saalwächter, K. Proton Multiple-Quantum NMR for the Study of Chain Dynamics and Structural Constraints in Polymeric Soft Materials. *Prog. NMR Spectrosc.* **2007**, *51*, 1–35.

(32) Ball, R. C.; Callaghan, P. T.; Samulski, E. T. A Simplified Approach to the Interpretation of Nuclear Spin Correlations in Entangled Polymeric Liquids. *J. Chem. Phys.* **1997**, *106*, 7352–7361.

(33) Wang, Z.; Likhtman, A. E.; Larson, R. G. Segmental Dynamics in Entangled Linear Polymer Melts. *Macromolecules* **2012**, *45*, 3557–3570.

(34) Fatkullin, N.; Gubaidullin, A.; Stapf, S. Features of Polymer Chain Dynamics As Revealed by Intermolecular Nuclear Magnetic Dipole-Dipole Interaction: Model Calculations and Field-Cycling NMR Relaxometry. *J. Chem. Phys.* **2010**, *132*, 094903.

(35) Meier, R.; Kahlau, R.; Kruk, D.; Rössler, E. A. Comparative Studies of the Dynamics in Viscous Liquids by Means of Dielectric

Spectroscopy and Field Cycling NMR. *J. Phys. Chem. A* **2010**, *114*, 7847–7855.

(36) Fatkullin, N.; Gubaidullin, A.; Mattea, C.; Stapf, S. On the Theory of the Proton Free Induction Decay and Hahn Echo in Polymer Systems: The Role of Intermolecular Magnetic Dipole-Dipole Interactions and the Modified Anderson–Weiss Approximation. *J. Chem. Phys.* **2012**, *137*, 224907.

(37) Fatkullin, N.; Mattea, C.; Stapf, S. On the Theory of Double Quantum NMR in Polymer Systems: The Second Cumulant Approximation for Many Spin  $I=1/2$  Systems. *J. Chem. Phys.* **2013**, *139*, 194905.

(38) Vaca Chávez, F.; Saalwächter, K. Time-Domain NMR Observation of Entangled Polymer Dynamics: Analytical Theory of Signal Functions. *Macromolecules* **2011**, *44*, 1560–1569.

(39) van Heukelum, A.; Barkema, G. T. Reaching Large Lengths and Long Times in Polymer Dynamics Simulations. *J. Chem. Phys.* **2003**, *119*, 8197–8203.

(40) Panja, D.; Barkema, G. T. Rouse Modes of Self-Avoiding Flexible Polymers. *J. Chem. Phys.* **2009**, *131*, 154903.

(41) Klein Wolterink, J.; Barkema, G. T.; Panja, D. Passage Times for Unbiased Polymer Translocation through a Narrow Pore. *Phys. Rev. Lett.* **2006**, *96*, 208301.

(42) Panja, D.; Barkema, G. T.; Ball, R. C. Anomalous Dynamics of Unbiased Polymer Translocation through a Narrow Pore. *J. Phys.: Condens. Matter* **2007**, *19*, 432202.

(43) Vocks, H.; Panja, D.; Barkema, G. T.; Ball, R. C. Pore-Blockade Times for Field-Driven Polymer Translocation. *J. Phys.: Condens. Matter* **2008**, *20*, 095224.

(44) Panja, D.; Barkema, G. T. Passage Times for Polymer Translocation Pulled through a Narrow Pore. *Biophys. J.* **2008**, *94*, 1630–1637.

(45) Panja, D.; Barkema, G. T.; Kolomeisky, A. B. Non-equilibrium Dynamics of Single Polymer Adsorption to Solid Surfaces. *J. Phys.: Condens. Matter* **2009**, *21*, 242101.

(46) Klein Wolterink, J.; Barkema, G. T.; Cohen Stuart, M. A. Diffusion and Exchange of Adsorbed Polymers Studied by Monte Carlo Simulations. *Macromolecules* **2005**, *38*, 2009–2014.

(47) Walter, J.-C.; Barkema, G. T.; Carlon, E. The Equilibrium Winding Angle of a Polymer around a Bar. *J. Stat. Mech.* **2011**, P10020.

(48) Walter, J.-C.; Baiesi, M.; Barkema, G. T.; Carlon, E. Unwinding Relaxation Dynamics of Polymers. *Phys. Rev. Lett.* **2013**, *110*, 068301.

(49) Schram, R. D.; Barkema, G. T.; Schiessel, H. On the Stability of Fractal Globules. *J. Chem. Phys.* **2013**, *138*, 224901.

(50) Mark, J. E., Ed.; *Physical Properties of Polymers Handbook*; Springer: New York, 2007.

(51) Klopffer, M.-H.; Bokobza, L.; Monnerie, L. Effect of Vinyl Content on the Viscoelastic Properties of Polybutadienes and Polyisoprenes—Monomeric Friction Coefficient. *Polymer* **1998**, *39*, 3445–3449.

(52) Baum, J.; Pines, A. NMR Studies of Clustering in Solids. *J. Am. Chem. Soc.* **1986**, *108*, 7447–7454.

(53) Klinkenberg, M.; Blümli, P.; Blümli, B. H-2-NMR Imaging of Stress in Strained Elastomers. *Macromolecules* **1997**, *30*, 1038–1043.

(54) Navon, G.; Shinar, H.; Eliav, U.; Seo, Y. Multiquantum Filters and Order in Tissues. *NMR Biomed.* **2001**, *14*, 112–132.

(55) Lorthioir, C.; Randriamahefa, S.; Deloche, B. Some Aspects of the Orientational Order Distribution of Flexible Chains in a Diblock Mesophase. *J. Chem. Phys.* **2013**, *139*, 224903.

(56) Schneider, M.; Gasper, L.; Demco, D. E.; Blümli, B. Residual Dipolar Couplings by  $^1\text{H}$  Dipolar-Encoded Longitudinal Magnetization, Double- and Triple-Quantum Nuclear Magnetic Resonance in Cross-Linked Elastomers. *J. Chem. Phys.* **1999**, *111*, 402–415.

(57) Saalwächter, K.; Herrero, B.; López-Manchado, M. A. Chain Order and Crosslink Density of Elastomers As Investigated by Proton Multiple-Quantum NMR. *Macromolecules* **2005**, *38*, 9650–9660.

(58) Panja, D. Generalized Langevin Equation Formulation for Anomalous Polymer Dynamics. *J. Stat. Mech.* **2010**, L02001.

- (59) Panja, D. Anomalous Polymer Dynamics Is Non-Markovian: Memory Effects and The Generalized Langevin Equation Formulation. *J. Stat. Mech.* **2010**, P06011.
- (60) Carmesin, I.; Kremer, K. The Bond Fluctuation Model: A New Effective Algorithm for the Dynamics of Polymers in All Spatial Dimensions. *Macromolecules* **1988**, *21*, 2819–2823.
- (61) Saalwächter, K. Comment on “Chain Entanglements in Polyethylene Melts. Why Is It Studied Again? *Macromolecules* **2013**, *46*, 5090–5093.
- (62) Allen, M. P. Tildesley, D. T. *Computer Simulation of Liquids*; Oxford University Press: New York, 1987.
- (63) Panja, D.; Barkema, G. T.; Ball, R. C.. Complex Interactions with the Surroundings Dictate a Tagged Chain’s Dynamics in a Polymer Melt. Manuscript in preparation.
- (64) Hintermeyer, J.; Herrmann, A.; Kahlau, R.; Goiceanu, C.; Rössler, E. A. Molecular Weight Dependence of Glassy Dynamics in Linear Polymers Revisited. *Macromolecules* **2008**, *41*, 9335–9344.
- (65) Schröter, K.; Hutcheson, S. A.; Shi, X.; Mandanici, A.; McKenna, G. B. Dynamic Shear Modulus of Glycerol: Corrections Due to Instrument Compliance. *J. Chem. Phys.* **2006**, *125*, 214507.
- (66) Blochowicz, T. Broadband Dielectric Spectroscopy in Neat and Binary Molecular Glass Formers. Frequency and Time Domain Spectroscopy, Non-Resonant Spectral Hole Burning. Dissertation, Universität Bayreuth, 2003.